Measurement of Optical Feshbach Resonances in an Ideal Gas

S. Blatt,[1] T. L. Nicholson,[1] B. J. Bloom,[1] J. R. Williams,[1] J. W. Thomsen,[1,*] P. S. Julienne,[2] and J. Ye[1]

[1]JILA and Department of Physics, NIST and University of Colorado, Boulder, Colorado 80309-0440, USA
[2]Joint Quantum Institute, NIST and the University of Maryland, Gaithersburg, Maryland 20899-8423, USA

(Received 31 March 2011; published 12 August 2011)

Using a narrow intercombination line in alkaline earth atoms to mitigate large inelastic losses, we explore the optical Feshbach resonance effect in an ultracold gas of bosonic ^{88}Sr. A systematic measurement of three resonances allows precise determinations of the optical Feshbach resonance strength and scaling law, in agreement with coupled-channel theory. Resonant enhancement of the complex scattering length leads to thermalization mediated by elastic and inelastic collisions in an otherwise ideal gas. Optical Feshbach resonance could be used to control atomic interactions with high spatial and temporal resolution.

DOI: 10.1103/PhysRevLett.107.073202 PACS numbers: 34.50.Rk, 34.50.Cx, 32.80.Qk

The ability to control the strength of atomic interactions has led to explosive progress in the field of quantum gases for studies of few- and many-body quantum systems. This capability is brought about by magnetic field-induced Feshbach scattering resonances (MFRs) [1], where both the magnitude and sign of low-energy atomic interactions can be varied by coupling free particles to a molecular state. MFRs in ultracold alkali atoms have been used to realize novel few-body quantum states and study strongly correlated many-body systems and phase transitions [1,2]. However, magnetic tuning has limited current experiments to relatively slow time scales and low spatial resolution. Higher resolution could be achieved by controlling MFRs optically [3].

Scattering resonances can also arise under the influence of laser light tuned near a photoassociation (PA) resonance [4], where free atom pairs are coupled to an excited molecular state [5,6]. This optical Feshbach resonance (OFR) is expected to enable new and powerful control with high spatial and temporal resolution. OFR has been studied in thermal [7] and degenerate [8,9] gases of Rb, but it was not found useful due to large PA losses. Much narrower optical intercombination lines are available in alkaline earth atoms and are predicted to overcome this loss problem [10]. Independently, ultracold alkaline earth atoms have recently emerged to play leading roles for quantum metrology [11–13], where precision measurement and many-body quantum systems are combined to study new quantum phenomena [14,15]. Degenerate gases of alkaline earth atoms have recently become available [16]. Because of the lack of magnetic structure in the ground state of these atoms, the OFR effect could become an important tool for controlling their interactions. OFR work on Yb [17,18] has been limited to studying the induced change in scattering phase shifts and PA rates. Dominant PA losses are evident in all of the OFR experiments listed above. Light-induced elastic collisions for thermalization were not observed.

In this Letter, we study the OFR effect across multiple resonances in a metastable molecular potential of ^{88}Sr. The aim of this work is to test the practical applicability of OFR for engineering atomic interactions in the presence of loss, similar to the successful application of a decaying MFR [19]. For ^{88}Sr, OFR is predicted [10] to allow changes in the scattering length by more than a factor of 100 with low losses by using large detunings [$O(10^5)$ linewidths] from the least-bound vibrational level [20]. We tested this proposal and find experimentally that the existing isolated resonance model [6] describes the experiment only in the small detuning regime. Large detunings from a molecular resonance require a full coupled-channel description of the molecular response. Supported by this new theory framework, we present a systematic experimental study of the OFR-enhanced complex scattering lengths and demonstrate OFR-induced thermalization in an ultracold gas.

Bosonic ^{88}Sr has an s-wave background scattering length $a_{\mathrm{bg}} = -1.4(6)a_0$ [21], where a_0 is the Bohr radius. The small $|a_{\mathrm{bg}}|$ makes the sample effectively noninteracting and provides an ideal testing environment for OFR. Figure 1(a) shows the ground ($^1S_0 - {}^1S_0$ 0_g) and lowest excited state ($^1S_0 - {}^3P_1$ 0_u) molecular potentials of Sr_2, which are coupled by a PA laser near the atomic transition at $\lambda_a = 689$ nm. The vibrational levels investigated are labeled by their quantum number n, counted as negative integers from the free particle threshold. For a given PA laser detuning from threshold, the Franck-Condon principle localizes the atom-light interaction in the vicinity of the Condon point [6].

When detuning the PA laser across a vibrational resonance, the s-wave scattering length shows a dispersive behavior, just as for a MFR. However, the finite lifetime of the excited molecular state leads to loss intrinsic to OFR. This process can be described [22] akin to a decaying MFR [1,19] with a complex s-wave scattering length $\alpha(k) \equiv a(k) - ib(k)$ that depends on the relative momentum $\hbar k$ and a PA line strength factor $\ell_{\mathrm{opt}} = \frac{\lambda_a^3}{16\pi c}\frac{|\langle n|E\rangle|^2}{k} I$, called the optical length [10,23]. Here, c is the speed of light, and ℓ_{opt} scales linearly with PA intensity I and

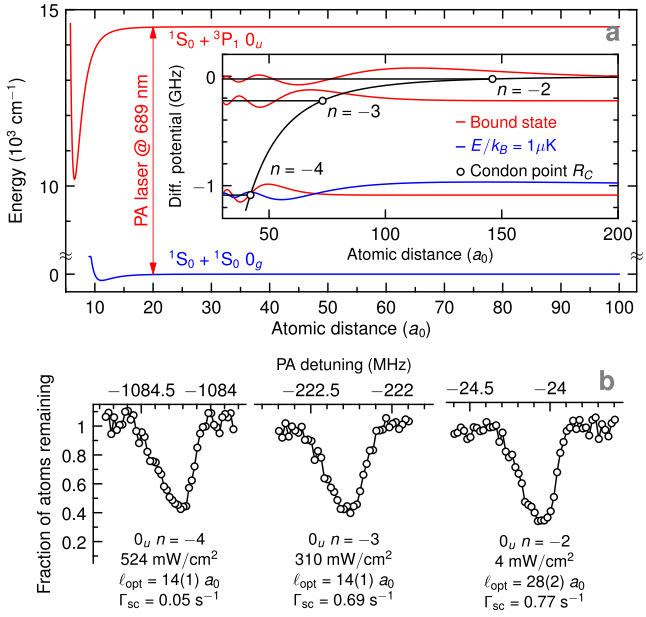

FIG. 1 (color online). (a) Ground (blue lines) and excited (red lines) molecular potentials of Sr_2. The inset shows the difference potential after subtracting the optical frequency. Horizontal lines indicate bound molecular states n in the excited potential. The free particle (bound state) radial wave function is indicated in blue (red). (b) Loss spectra for 0_u $n = -2$, -3, and -4 for exposure time $\tau_{PA} = 200$ ms and comparable mean density. I is scaled to keep Γ_{sc} sufficiently small. The similarity of the spectra demonstrates the universal scaling with $\ell_{opt} \propto |\langle n|E\rangle|^2 I$.

free-bound Franck-Condon factor $|\langle n|E\rangle|^2$ per unit collision energy $E = \hbar^2 k^2/(2\mu)$ at reduced mass $\mu = m_{Sr}/2$. In the isolated resonance approximation [6], the inelastic rate constant is [22]

$$K_{in}(k) = \frac{4\pi\hbar}{\mu} \frac{\frac{\ell_{opt}\gamma_m}{\gamma}}{(\Delta + E/\hbar)^2/\gamma^2 + [1 + 2k\frac{\ell_{opt}\gamma_m}{\gamma}]^2/4}, \quad (1)$$

where Δ is the laser detuning from molecular resonance [22]. We have accounted for extra molecular losses with $\gamma > \gamma_m = 2\gamma_a$, where γ_m is the linewidth of the molecular transition and $\gamma_a = 2\pi \times 7.5$ kHz is the atomic linewidth. Neglecting a_{bg} for ^{88}Sr gives $K_{el}(k) \simeq 2k\frac{\ell_{opt}\gamma_m}{\gamma} K_{in}(k)$. The elastic-to-inelastic collision ratio K_{el}/K_{in} becomes less favorable for smaller k.

We load $\sim 5 \times 10^4$ atoms from a magneto-optical trap operating on the $^1S_0 - {}^3P_1$ intercombination transition into a crossed optical dipole trap formed by tilted horizontal (H) and vertical (V) beams (1064 nm), with trap depths $\sim$15 and $\sim$7 μK, respectively. The trapped sample shows a clear kinetic energy inhomogeneity between the H and V axes (2–2.5 μK vs 3–4 μK), due to the negligible a_{bg}, consistent with a thermal distribution that is energy filtered by the trap potential. Typical in-trap cloud diameters are 45–55 μm. The PA beam intersects the trap with a waist of 41 μm [22].

A representative survey of PA resonances in the $^1S_0 - {}^3P_1\ 0_u$ potential is shown in Fig. 1(b). The PA laser with intensity I, adjusted to achieve similar ℓ_{opt} for all spectra shown, interacts with the sample for τ_{PA}. Photon-atom scattering at rate Γ_{sc} and subsequent radiation trapping set the maximum usable I for a given detuning from the atomic line [22]. In addition to the vibrational levels indicated in Fig. 1(a), the $n = -1$ vibrational state exists at -0.4 MHz detuning from the threshold, which leads to a PA resonance with a very large line strength ℓ_{opt}/I [20]. The isolated resonance theory indicates that operating with a large I at $O(10^5\gamma_a)$ detuning from the $n = -1$ state should allow modifications to $a(k)$ of $O(100a_0)$ [10]. This prediction relied on extrapolating the large line strength of the $n = -1$ state across multiple intermediate PA resonances. However, with I up to 1 kW/cm^2 and detunings up to -1.5 GHz, we did not observe any effects due to elastic collisions.

The discrepancy between theory and experiment stimulated a coupled-channel treatment of an atomic collision in a radiation field that properly switches between the short range molecular states and two field-dressed separated atoms [22,24,25]. In the coupled-channel theory, the two coupled excited potentials (0_u and 1_u) have the same form as in Ref. [20], with an added imaginary term $-i\hbar\gamma_m/2$. The ground state potential uses the dispersion coefficients of Ref. [26], has a scattering length of $-1.4a_0$, and reproduces the bound state data of Ref. [21] to better than 0.4%. Coupled-channel calculations do not assume isolated resonances, and all 0_u and 1_u molecular eigenstates emerge from the calculation as interfering, decaying scattering resonances [1].

Figures 2(c) and 2(d) show that the coupled-channel model reproduces the isolated resonance expressions [1,6] for $\alpha(k)$ and the rate constants as long as Δ is small compared to the spacing between molecular levels. However, the coupled-channel K_{el} returns to its background value K_{el}^{bg} in between resonances regardless of their relative strengths. The dotted line indicates K_{el}^{bg} (a_{bg}) at $E/k_B = 4$ μK in Fig. 2(a) [Fig. 2(d)]. These calculations show that each molecular line behaves as an isolated resonance near its line center. For detunings comparable to the molecular level spacing, the isolated resonance expressions cannot be used.

At intermediate detunings $|\Delta| \gg \gamma(1 + 2k\ell_{opt}\frac{\gamma_m}{\gamma})$, $\alpha(k)$ can be written in the standard form for MFRs [22]:

$$\lim_{k\to 0}\alpha(k) = a_{bg}\left(1 - \frac{w}{\Delta} + \frac{i}{2}\frac{w\gamma}{\Delta^2}\right), \quad (2)$$

where $w \equiv -\ell_{opt}\gamma_m/a_{bg}$. A meaningful change in scattering length requires a sufficiently large $\ell_{opt}\gamma_m/\Delta$ and a sufficiently small imaginary part $b = \frac{1}{2}\ell_{opt}\gamma_m\gamma/\Delta^2$. Since $K_{in} \simeq (2 \times 10^{-12}$ cm^3/s$)(b/a_0)$, for a density of $\rho = 10^{12}$ cm^{-3} and $b = 2.5a_0$, $K_{in}\rho = \Gamma_{sc}$ for $I = 53$ W/cm^2 assumed for Figs. 2(c) and 2(d). Thus, the calculations

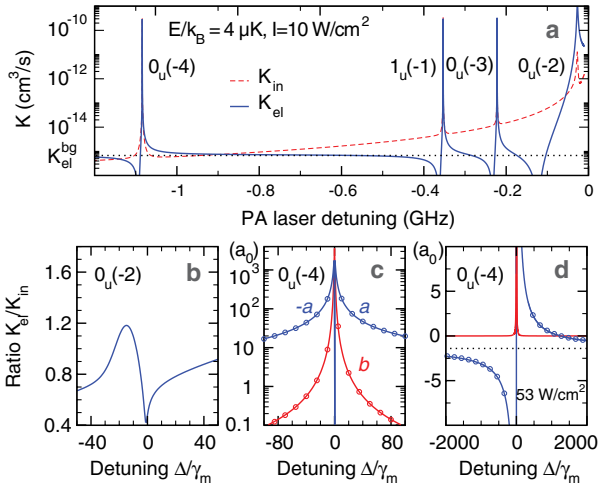

FIG. 2 (color online). (a) Coupled-channel calculations of $K_{\rm el}$ and $K_{\rm in}$ at $E/k_B = 4\ \mu$K and $I = 10$ W/cm^2 versus PA laser detuning from atomic resonance. Each resonance peak is labeled by its electronic symmetry 0_u or 1_u and n. Between resonances, $K_{\rm in}$ is proportional to $\Gamma_{\rm sc}$. (b) Ratio of thermally averaged rate constants at 2 μK for Δ/γ_m near $0_u(-2)$. $I = 44$ mW/cm^2 gives the same $\ell_{\rm opt} = 360a_0$ as for Fig. 4(b). (c),(d) Zero energy limit of $a(k)$ and $b(k)$ for the $0_u(-4)$ feature. The isolated resonance results (solid lines) agree with the coupled-channel theory (circles).

predict that changes in the scattering length of order $90a_0 \gg |a_{\rm bg}|$ should be possible with $O(20\gamma_m)$ detunings on time scales of 200 ms.

To investigate the utility of OFR, we systematically characterized three different resonances and determined their universal scaling. Because $K_{\rm el}/K_{\rm in} \propto k\ell_{\rm opt}$, inelastic collisions dominate the dynamics of the sample for small $\ell_{\rm opt} \ll (2\langle k\rangle)^{-1} = \frac{\hbar}{2}\sqrt{\pi/(8\mu k_B T)}$, where the angled brackets indicate a k average at temperature T and k_B is the Boltzmann constant. In this regime, the result of scanning the PA laser across resonance is a loss feature that shows no dependence on elastic collision processes.

A typical PA loss feature for small $\ell_{\rm opt}$ is shown in Fig. 3(a), where the final atom number after application of PA light is shown with respect to PA detuning from $^1S_0 - {}^3P_1$. The per-axis kinetic energies [22] for this scan correspond to a horizontal (vertical) temperature T_H (T_V) $= 2\ \mu$K (3 μK), resulting in the typical thermal tail towards the red side of the resonance [27]. The solid line is a result of solving a two-body rate equation [20,22], with a vacuum-limited trap lifetime 1.3 s and a thermally averaged $K_{\rm in}$. Figure 3(b) shows the time dependence of the two-body PA loss process.

From the experimental data we extract two independent quantities: $\ell_{\rm opt}\gamma_m$ and an increased molecular loss rate $\gamma \simeq 2.7\gamma_m$. Ruling out magnetic field or PA laser noise, we conclude that the broadening is related to a faster molecular decay rate, consistent with our earlier measurements [20] and Rb results [8].

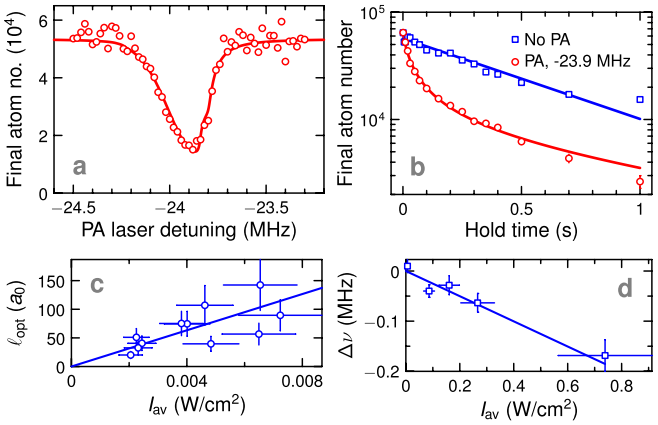

n	theory $\ell_{\rm opt}/I$ ($\frac{a_0}{\rm W/cm^2}$)	experiment $\ell_{\rm opt}/I_{\rm av}$ ($\frac{a_0}{\rm W/cm^2}$)	$\frac{\gamma_m}{\gamma}\ell_{\rm opt}/I_{\rm av}$ ($\frac{a_0}{\rm W/cm^2}$)	ν_n (MHz)	$\Delta\nu/I_{\rm av}$ ($\frac{\rm kHz}{\rm W/cm^2}$)
-2	8.3×10^3	$15.8(8) \times 10^3$	$5.9(3) \times 10^3$	-23.98(1)	$-(251 \pm 67)$
-3	38	68(3)	26(1)	-222.18(5)	$+(29 \pm 2)$
-4	32	40(2)	15(1)	-1084.12(5)	$+(4 \pm 1)$

FIG. 3 (color online). (a) Typical PA loss feature for $n = -2$ in the low intensity regime at $I_{\rm av} = 7$ mW/cm^2, with density-profile-averaged PA intensity $I_{\rm av}$ [22]. (b) Time evolution of the trapped sample with (circles) and without (squares) PA light. The two-body loss curve with PA is fit with a thermally averaged model (solid curve). (c) Linear increase of $\ell_{\rm opt}$ with $I_{\rm av}$ for $\ell_{\rm opt} \ll 1/(2\langle k\rangle)$. (d) Molecular line center shift $\Delta\nu$ for large $I_{\rm av}$ and decreased $\tau_{\rm PA}$. For each n, OFR parameters from the coupled-channel calculation and the experiment are summarized in the table at the bottom. Here, ν_n is the zero-intensity molecular line center with respect to $^1S_0 - {}^3P_1$, and $\Delta\nu/I_{\rm av}$ characterizes the molecular ac Stark shift [23].

The measurements were performed for a range of $\ell_{\rm opt}$ by adjusting $I_{\rm av}$. Multiple molecular resonances were measured, and results for $n = -2$ are shown in Fig. 3(c). The optical length data are fit with a linear function, and the results are summarized in the table at the bottom. The fit coefficient $\ell_{\rm opt}/I_{\rm av}$ is given by the free-bound Franck-Condon factor and decreases drastically with decreasing n. Figure 3(d) exemplifies similar measurements done to determine the line shift $\Delta\nu$ with $I_{\rm av}$. Linear shift coefficients $\Delta\nu/I_{\rm av}$ and zero-intensity line positions ν_n with respect to the atomic transition are also shown in the table. The sign and magnitude of $\Delta\nu/I_{\rm av}$ are consistent with the predictions in Ref. [23].

At larger optical lengths ($\ell_{\rm opt}\gamma_m/\gamma \sim 100a_0$), elastic collisions start to influence the dynamics of the system. We show the atom loss with respect to PA laser detuning for $n = -2$ in Fig. 4(a). Both in-trap size and kinetic energy are measured by absorption imaging [22]. Far detuned from the resonance, the gas is almost ideal, as shown by the persistent kinetic energy inhomogeneity along H and V in Fig. 4(b). On resonance (vertical dashed line), inelastic collisions dominate and cause heating. For red detuning from the molecular resonance, the temperatures approach each other by cross-thermalization [28].

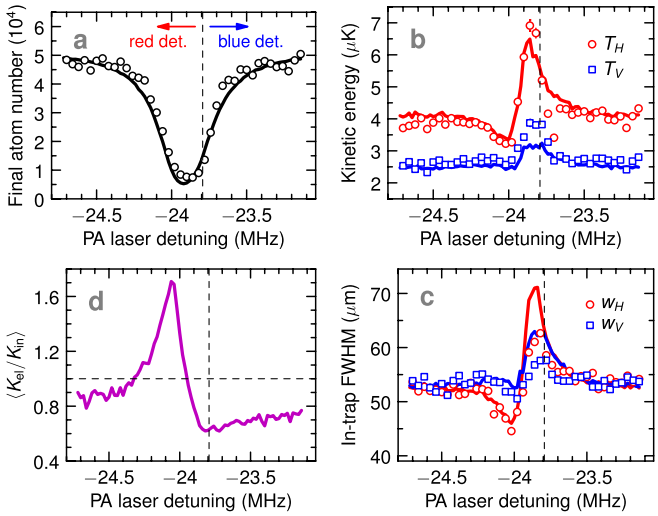

FIG. 4 (color online). Elastic contribution to the scattering cross section for $n = -2$ at $I_{\mathrm{av}} = 22\ \mathrm{mW/cm^2}$ (open circles) and results of a Monte Carlo simulation (solid lines) using Eq. (1) in a crossed dipole trap for $\ell_{\mathrm{opt}}\gamma_m/\gamma = 140a_0$. (a) Atom loss as a function of PA laser detuning from the atomic $^1S_0 - {}^3P_1$ resonance. In (b) and (c), blue (red) data points and solid lines indicate the corresponding quantities for the vertical (horizontal) trap axis. (b) Change in kinetic energy derived from time-of-flight images, and (c) potential energy change corresponding to a varying in-trap density profile. (d) The resulting ratio of elastic and inelastic collisions per particle, averaged over τ_{PA}.

The measured cloud widths w_H and w_V confirm that the potential energy follows the kinetic energy [Fig. 4(c)] since particles oscillate in the trap many times between collisions. Similar measurements were performed for $n = -3$ and $n = -4$, and we find that the same dispersive behavior in temperatures and widths appears around $2\langle k\rangle\ell_{\mathrm{opt}}\gamma_m/\gamma \sim 30\%$ at $\tau_{\mathrm{PA}} = 200$ ms. The data can be understood by a simple picture of competition between K_{el} and K_{in}, which average differently with k in a thermal sample [see Eq. (1)] and thus peak at different values of Δ. Elastic collisions cause cross-dimensional thermalization and tend to equalize T_H and T_V. Since inelastic collisions predominantly remove cold atoms from the densest part of the cloud, the resulting loss increases the average system energy via antievaporation.

This behavior is confirmed by a Monte Carlo simulation, where 55×10^3 particles are simulated and each particle undergoes elastic and inelastic collisions with an initial phase-space distribution matched to the experimental conditions [22]. The solid lines overlaid on the experimental data in Fig. 4 are the simulation results. An average ratio of elastic to inelastic collisions per particle from the simulation is shown in Fig. 4(d). The dispersive shapes are also predicted by the coupled-channel model [see Fig. 2(b)], and their shape is sensitive to γ. Combined with the low ℓ_{opt} data in Fig. 3, the entire simulation reproduces the experimental data only when $\gamma = 2\pi \times 40(5)$ kHz without other free parameters.

We conclude that the isolated resonance approximation universally describes OFR in the vicinity of each resonance. The coupled-channel calculation includes all interference effects between resonances and differs from the isolated resonance approximation at large detuning between resonances. Our experiment contradicts previous predictions based on extrapolations of an isolated resonance to large detunings [10,20]. We have validated the linear line strength scaling and linear resonance shift with I and have observed a clear modification of both $a(k)$ and $b(k)$. For the values of $\ell_{\mathrm{opt}}\gamma_m/\gamma$ achieved here, inelastic losses still contribute significantly and $\langle K_{\mathrm{el}}/K_{\mathrm{in}}\rangle$ becomes even less favorable with decreasing T. However, the OFR effect can modify interactions in a degenerate gas of alkaline earth atoms, and the desired change of $a(k)$ is achieved at the smallest Δ/γ constrained by both molecular and atomic loss processes over a given experimental time scale [22].

We thank C. Greene, P. Zoller, and G. Campbell for discussions and contributions. J. R. W. received support from an NRC fellowship. Our work is funded by DARPA OLE, NIST, and NSF.

*Permanent address: The Niels Bohr Institute, Universitetsparken 5, 2100 Copenhagen, Denmark.

[1] C. Chin *et al.*, Rev. Mod. Phys. **82**, 1225 (2010).
[2] I. Bloch, J. Dalibard, and W. Zwerger, Rev. Mod. Phys. **80**, 885 (2008); S. Giorgini, L. P. Pitaevskii, and S. Stringari, *ibid.* **80**, 1215 (2008); W. Ketterle and M. W. Zwierlein, in *Ultracold Fermi Gases*, Proceedings of the International School of Physics "Enrico Fermi," Course CLXIV (Elsevier, Amsterdam, 2008), p. 95.
[3] D. M. Bauer *et al.*, Nature Phys. **5**, 339 (2009).
[4] K. Jones *et al.*, Rev. Mod. Phys. **78**, 483 (2006).
[5] P. Fedichev *et al.*, Phys. Rev. Lett. **77**, 2913 (1996).
[6] J. Bohn and P. Julienne, Phys. Rev. A **60**, 414 (1999).
[7] F. Fatemi, K. Jones, and P. Lett, Phys. Rev. Lett. **85**, 4462 (2000).
[8] M. Theis *et al.*, Phys. Rev. Lett. **93**, 123001 (2004).
[9] G. Thalhammer *et al.*, Phys. Rev. A **71**, 033403 (2005).
[10] R. Ciuryło, E. Tiesinga, and P. S. Julienne, Phys. Rev. A **71**, 030701 (2005).
[11] T. Akatsuka, M. Takamoto, and H. Katori, Nature Phys. **4**, 954 (2008).
[12] G. K. Campbell *et al.*, Science **324**, 360 (2009).
[13] N. Poli *et al.*, Phys. Rev. Lett. **106**, 038501 (2011).
[14] M. D. Swallows *et al.*, Science **331**, 1043 (2011).
[15] A. V. Gorshkov *et al.*, Nature Phys. **6**, 289 (2010).
[16] Y. Takasu *et al.*, Phys. Rev. Lett. **91**, 040404 (2003); S. Kraft *et al.*, Phys. Rev. Lett. **103**, 130401 (2009); S. Stellmer *et al.*, *ibid.* **103**, 200401 (2009); Y. de Escobar *et al.*, *ibid.* **103**, 200402 (2009).
[17] K. Enomoto *et al.*, Phys. Rev. Lett. **101**, 203201 (2008).
[18] R. Yamazaki *et al.*, Phys. Rev. Lett. **105**, 050405 (2010).

[19] D. Naik *et al.*, Eur. Phys. J. D (to be published).
[20] T. Zelevinsky *et al.*, Phys. Rev. Lett. **96**, 203201 (2006).
[21] Y. de Escobar *et al.*, Phys. Rev. A **78**, 062708 (2008).
[22] See Supplemental Material at http://link.aps.org/supplemental/10.1103/PhysRevLett.107.073202 for details.
[23] R. Ciuryło, E. Tiesinga, and P. S. Julienne, Phys. Rev. A **74**, 022710 (2006).
[24] P. Julienne and F. Mies, Phys. Rev. A **34**, 3792 (1986).
[25] R. Napolitano, J. Weiner, and P. S. Julienne, Phys. Rev. A **55**, 1191 (1997).
[26] S. G. Porsev and A. Derevianko, J. Exp. Theor. Phys. **102**, 195 (2006).
[27] R. Ciuryło *et al.*, Phys. Rev. A **70**, 062710 (2004).
[28] J. Goldwin *et al.*, Phys. Rev. A **71**, 043408 (2005).